

1 **Unleashing the Potential of Geostationary Satellite Observations in Air**
2 **Quality Forecasting Through Artificial Intelligence Techniques**

3 Chengxin Zhang¹, Xinhan Niu¹, Hongyu Wu², Zhipeng Ding², Ka Lok Chan³, Jhoon Kim⁴,
4 Thomas Wagner⁵, Cheng Liu^{1,6,7*}

5 ¹Department of Precision Machinery and Precision Instrumentation, University of Science and
6 Technology of China, Hefei, 230026, China

7 ²School of Environmental Science and Optoelectronic Technology, University of Science and
8 Technology of China, Hefei, 230026, China

9 ³Rutherford Appleton Laboratory Space, Harwell Oxford, United Kingdom

10 ⁴Department of Atmospheric Sciences, Yonsei University, Seoul, Republic of Korea

11 ⁵Satellite Remote Sensing Group, Max Planck Institute for Chemistry, Mainz, Germany

12 ⁶Key Laboratory of Environmental Optics and Technology, Anhui Institute of Optics and Fine
13 Mechanics, Chinese Academy of Sciences, Hefei, 230031, China

14 ⁷Key Laboratory of Precision Scientific Instrumentation of Anhui Higher Education Institutes,
15 University of Science and Technology of China, Hefei, 230026, China

16

17 *Correspondence: Cheng Liu (chliu81@ustc.edu.cn)

18

19

20 **Abstract.**

21 Air quality forecasting plays a critical role in mitigating air pollution. However, current
22 physics-based air pollution predictions encounter challenges in accuracy and spatiotemporal
23 resolution due to limitations in the understanding of atmospheric physical mechanisms,
24 observational constraints, and computational capacity. The world's first geostationary satellite
25 UV-Vis spectrometer, i.e., the Geostationary Environment Monitoring Spectrometer (GEMS),
26 offers hourly measurements of atmospheric trace gas pollutants at high spatial resolution over
27 East Asia. In this study, we successfully incorporate Geostationary satellite observations into
28 a neural network model (GeoNet) to forecast full-coverage surface nitrogen dioxide (NO₂)
29 concentrations over eastern China at 4-hour intervals for the next 24 hours. GeoNet leverages
30 spatiotemporal series of satellite NO₂ observations to capture the intricate relationships among
31 air quality, meteorology, and emissions in both temporal and spatial domains. Evaluation
32 against ground-based measurements demonstrates that GeoNet accurately predicts diurnal
33 variations and spatial distribution details of next-day NO₂ pollution, yielding the coefficient of
34 determination of 0.68 and root mean square of error of 12.31 μg/m³, significantly surpassing
35 traditional air quality model forecasts. The model's interpretability reveals that geostationary
36 satellite observations notably improve NO₂ forecast capability more than other input features,
37 especially over polluted regions. Our findings demonstrate the significant potential of
38 geostationary satellite observations in artificial intelligence-based air quality forecasting, with
39 implications for early warning of air pollution events and human health exposure.

40 **Keywords:** air quality forecast; deep learning; health impact; satellite remote sensing;
41 nitrogen dioxide;

42 **1 Introduction**

43 Since the industrial revolution, numerous countries worldwide have encountered severe
44 air pollution issues such as photochemical ozone smog and haze pollution (Hong et al., 2019),
45 which significantly affect human health, crop yields, and the global environment (Manisalidis
46 et al., 2020; Sathe et al., 2021; Guarin et al., 2024). Recent studies have shown that both long-
47 term and short-term exposure to air pollutants such as nitrogen dioxide (NO₂) can significantly
48 affect human health, especially the respiratory system (Meng et al., 2021). Accurate and high
49 spatial resolution predictions of air pollutant concentrations can provide critical information
50 for sensitive persons to mitigate health risks. Meanwhile, air quality health risk (AQHI)
51 forecasts and corresponding public response recommendations need to be communicated to the
52 public promptly through public facilities (Tang et al., 2024; Fino et al., 2021). In recent decades,
53 the advancement of atmospheric monitoring and modeling has enabled significant progress in
54 air quality forecasting based on our understanding of atmospheric physics and chemistry
55 (Peuch et al., 2022). Air pollution forecasting not only facilitates responses to environmental
56 health risks but also improves the accuracy of climate and weather simulations (Makar et al.,
57 2015). However, due to our still limited understanding of atmospheric mechanisms and
58 observational and emission constraints, existing air quality forecasts based on physical or
59 statistical models still face challenges in terms of temporal, spatial, and accuracy aspects
60 (Campbell et al., 2022; Zhong et al., 2021).

61 Artificial Intelligence (AI) technology has made breakthroughs in the field of Earth
62 science (Zhong et al., 2021; Boukabara et al., 2020), particularly excelling in addressing
63 complex problems that are challenging for traditional physical paradigms to simulate (Irrgang
64 et al., 2021), such as weather and climate forecasting (Andersson et al., 2021). Concerning
65 meteorological data, some large-scale deep learning models have surpassed the predictive
66 capabilities of existing numerical weather models to some extent, examples include Climax

67 (Nguyen et al., 2023), Pangu-Weather (Bi et al., 2023), and GraphCast (Lam et al., 2023).
68 Despite significant progress and impressive performance achieved in meteorological variables
69 forecasting with AI methods, there are still limitations in predicting atmospheric pollutant
70 compositions. Compared to meteorological parameters, the prediction of air pollutant
71 concentrations is affected by synoptic meteorology, chemistry, and anthropogenic emission
72 activities, usually with more complex driven mechanisms and associated uncertainties. Current
73 AI-based air quality forecasts often involve time series predictions at a limited number of
74 observation stations, rather than full-coverage predictions over the entire spatial domain (Du
75 et al., 2021). This is primarily due to the lack of effective air quality observations with high
76 temporal and spatial resolution simultaneously.

77 While past polar-orbiting satellite observations such as the Ozone Monitoring Instrument
78 (OMI) and the TROPospheric Monitoring Instrument (TROPOMI), have provided extensive
79 coverage of atmospheric pollutant distributions such as nitrogen dioxide (NO₂), sulfate dioxide
80 (SO₂), ozone (O₃), and aerosols, they are limited to once-daily overpasses and usually affected
81 by clouds (Van Geffen et al., 2022; Chan et al., 2023). This frequency usually exceeds the
82 chemical lifetimes of many reactive gas pollutants like NO₂, making it challenging to offer
83 effective observational constraints for machine learning short-term air quality forecasting
84 (Shah et al., 2020). However, these observations at a fixed daily overpass time could hardly
85 support the prediction of atmospheric trace gas concentrations at other times of the day under
86 different meteorological conditions. In February 2020, the world's first geostationary satellite
87 payload for air pollution monitoring, the Geostationary Environment Monitoring Spectrometer
88 (GEMS), began to provide high-coverage and high-precision air quality observations at an
89 hourly rate for the East Asian region (Kim et al., 2020). The dynamic processes of air pollutants
90 including emission, transformation, and transport can be observed by the geostationary satellite
91 during the daytime. This monitoring capability may advance data-driven air quality forecasting

92 such as machine learning techniques by offering unprecedented observational constraints with
93 high spatial and temporal coverage. Recent observing system simulation experiments (OSSE)
94 indicate that assimilating trace gas observations by geostationary satellites into chemical
95 models can effectively improve surface ozone simulations (Shu et al., 2023), nitrogen oxides
96 (NO_x), and emission estimates (Hsu et al., 2024).

97 Here, based on the unprecedented temporal and spatial resolution and coverage of the
98 GEMS satellite (Kim et al., 2020), we incorporated Geostationary satellite remote sensing of
99 tropospheric NO_2 column densities (refer to section 4 for details) into a neural Network model
100 (GeoNet), to forecast full-coverage surface NO_2 concentration over the next day from the
101 current time t (i.e., $t+24\text{h}$). Compared with previous air quality forecasting based on the
102 simulation of atmospheric physics and chemistry possibly combined with data assimilation
103 approaches, GeoNet relies solely on geostationary satellite measurements and ancillary
104 meteorology data. GeoNet effectively addresses the complex nonlinear relationships between
105 future short-term air quality and current satellite observations, as well as temporally adjacent
106 meteorological variables (Zhang et al., 2022). The method employs satellite and meteorological
107 variables within the spatial vicinity of individual air quality monitoring sites as input features,
108 with site observations serving as labels for model training. The resulting model achieves
109 accurate and comprehensive air quality predictions across the entire domain over East China,
110 which is a significant achievement given that past machine learning technologies have relied
111 on only a few stations or polar-orbiting satellite observations.

112 **2 Materials and Methods**

113 **2.1 Geostationary satellite observations of atmospheric NO_2**

114 GEMS is the first UV-Vis spectrometer at a geostationary satellite orbit, measuring
115 atmospheric pollutants such as NO_2 , SO_2 , O_3 , and HCHO over East Asia, at a spatial resolution
116 of $3.5 \text{ km} \times 7.5 \text{ km}$ at nadir and a temporal resolution of 1 hour during the daytime (Kim et al.,

117 2020). Based on the unique spectral absorption of trace gases, the atmospheric NO₂ column
118 can be retrieved in visible wavelengths from the spectra of back-scattered sunlight. The details
119 of the GEMS NO₂ retrieval can be found in the Algorithm Theoretical Basis Document
120 (available at <https://nesc.nier.go.kr/ko/html/satellite/doc/doc.do>, last access: June 1, 2023). In
121 this study, we used the tropospheric NO₂ column from the GEMS NO₂ version 2.0 product, as
122 well as the cloud fraction for each satellite ground pixel. Overall, GEMS NO₂ measurements
123 have a good correlation with ground-based remote sensing instruments, with correlation
124 coefficients (R) between 0.69-0.81, and root mean square of errors (RMSE) between 3.2-
125 4.9×10^{15} molecules/cm² (Kim et al., 2023). Our previous validation results indicated that
126 GEMS NO₂ retrievals generally agreed well with ground-based MAX-DOAS measurements
127 from 6 sites in China, with correlation coefficients ranging between 0.69-0.92 (Li et al., 2023).

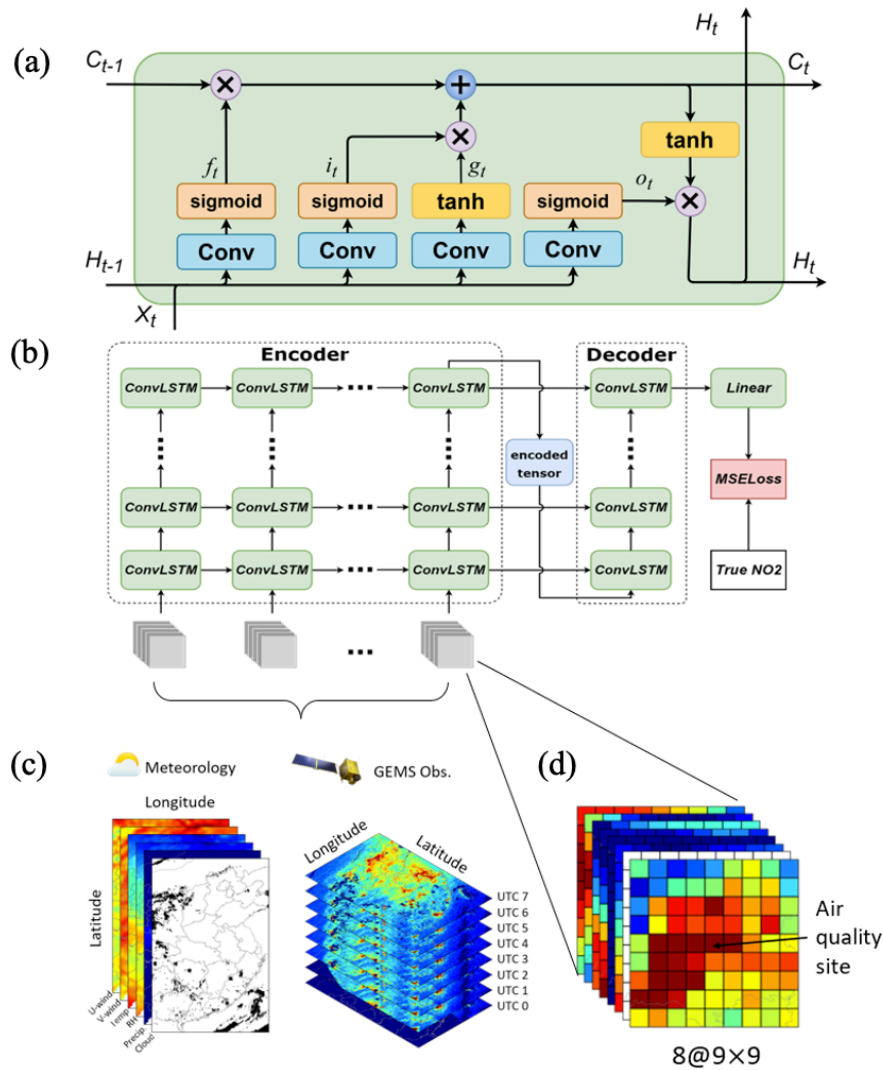
128 **2.2 Ancillary datasets**

129 Other input information including meteorological datasets is necessary to better constrain
130 the prediction of future NO₂ pollution. Here, both the ERA5 meteorology reanalysis (Hersbach
131 et al., 2020) and the CAMS forecast (Peuch et al., 2022) were used to provide meteorological
132 parameters such as zonal and meridional wind (U-wind and V-wind), temperature (Temp),
133 relative humidity (RH), and precipitation (Precip). In addition, the fraction of cloud cover
134 available from the satellite NO₂ datasets was also considered. To fill the missing gaps in the
135 satellite NO₂ measurements, we use both the NO₂ concentrations from the WRF-Chem model
136 (Zhang et al., 2022) and the CAMS forecast of atmospheric composition. Note that the
137 reanalysis datasets were typically updated with a week delay from real-time, while the forecast
138 datasets can provide future 7-day meteorology from the current time. Therefore, the latency of
139 input datasets would affect the operational prediction of the GeoNet model. Surface NO₂
140 measurements were used as the ground-truth label in the model training phase, available from

141 over 1000 national air quality sites by the China National Environmental Monitoring Centre
 142 (CNEMC) (Kong et al., 2021).

143 The preprocessing steps of model input datasets, including outlier detection, missing value
 144 handling, resampling, and normalization, are described in Supplementary Text S1.

145 **2.3 The GeoNet model**



146

147 **Figure 1.** The framework of predicting surface NO₂ map based on Geostationary satellite measurements and
 148 a ConvLSTM neural network model (GeoNet). (a) the structure of the ConvLSTM block; (b) a diagram of
 149 GeoNet model structure with inputs and output; (c) an illustration of the model input parameters including
 150 meteorological variables and hourly NO₂ measurements by the Geostationary satellite; (d) the input data
 151 cube of different features for single training batch, which is centered at an air quality site.

152 Fig. 1 illustrates the structure and methodology of the artificial intelligence air quality
 153 forecasting model established in this study. Given the distinctive nature of spatiotemporal

154 sequence data for air quality, predictions must consider not only temporal relationships but also
 155 spatial correlations. The deep learning model employed in this research utilizes convolutional
 156 long short-term memory (ConvLSTM) as its kernel, a variant of the LSTM model designed for
 157 the time series forecasting (Lin et al., 2020). It incorporates a convolutional network structure
 158 to capture spatial features of three-dimensional inputs. Both input-to-state and state-to-state
 159 transitions involve convolutional structures. ConvLSTM determines the future state of a unit
 160 within a grid based on inputs from its local neighbors and past states, allowing it to effectively
 161 model the spatiotemporal dynamics of air quality. The ConvLSTM kernel structure employed
 162 in training is illustrated in Fig. 5a. Here, X_t represents the input at time t , H_t and H_{t-1} denote
 163 the outputs at times t and $t-1$, and C_t and C_{t-1} represent the states at times t and $t-1$. The
 164 computational process is as follows:

$$165 \quad i_t = \sigma(X_t * w_{xi} + H_{t-1} * w_{hi} + b_i) \quad (1)$$

$$166 \quad f_t = \sigma(X_t * w_{xf} + H_{t-1} * w_{hf} + b_f) \quad (2)$$

$$167 \quad o_t = \sigma(X_t * w_{xo} + H_{t-1} * w_{ho} + b_o) \quad (3)$$

$$168 \quad g_t = \tanh(X_t * w_{xg} + H_{t-1} * w_{hg} + b_g) \quad (4)$$

$$169 \quad C_t = f_t \times C_{t-1} + i_t \times g_t \quad (5)$$

$$170 \quad H_t = o_t \times \tanh(C_t) \quad (6)$$

171 Where the asterisk (*) represents the convolution operator, w is the convolution kernel, b is the
 172 offset, \tanh is the hyperbolic tangent function, and σ is the activation function of Sigmoid.

173 The model primarily consists of three components: an encoder, a decoder, and fully
 174 connected layers. Tropospheric NO₂ observations from the GEMS satellite for different
 175 consecutive hours within a day, along with corresponding meteorological forecast field data,
 176 serve as input features for model training. The encoder processes the spatiotemporal sequences
 177 of input features for the preceding 8 hours ($t-7h, t-6h, \dots, t$), which are then decoded by the
 178 decoder. The final output, representing NO₂ concentrations at 4-hour intervals for the next 24

179 hours ($t+4h$, $t+8h$, $t+12h$,..., $t+24h$), is produced through fully connected layers. The loss
180 function of mean squared error (MSE) is calculated by comparing the model output with the
181 actual values from station observations, and the model undergoes iterative training. In the
182 training task for a single station sample, the model utilizes continuous and distinct hourly
183 dynamic images of all variables within the spatiotemporal vicinity of the station as input (see
184 Fig. 1c-d). This effectively considers the intricate correlations in time and space between air
185 quality, satellite observations, and meteorological input features. We train the GeoNet model
186 with input features during the whole year of 2021. The training datasets were randomly selected
187 from 75% of the whole samples, while the remaining 25% were used as validation sets.

188 **2.4 The model configuration and optimization**

189 The model configurations and hyperparameters such as the optimizer, loss function, L1 or
190 L2 regularization, dropout, training steps, and epochs can make a difference to the model
191 performance including the prediction accuracy and generalizability. The performance metrics
192 such as the coefficient of determination (R^2), root mean square of error (RMSE), mean absolute
193 error (MAE), and mean absolute percentage error (MAPE), were used to diagnose the model
194 (see definition in Supplementary Text S2). Thus, several scenarios of model hyperparameters
195 have been tested during the model training phase. The model accuracy on validation datasets
196 and the learning rate curve were used to diagnose the model hyperparameters. The model
197 parameters mainly include the number of layers and the dimensions of the hidden layers, both
198 control the model's capacity. If the model capacity is relatively small, underfitting may occur;
199 overfitting may exist if it is too large. Therefore, selecting an appropriate model capacity is
200 crucial for improving model performance. During the pre-training process, the model is trained
201 by combining different numbers of layers and dimensions of the hidden layers. The Mean
202 Squared Error (MSE) Loss is recorded for each training iteration, and a heatmap is generated
203 as shown in Fig. S2. From the heatmap, it can be observed that when the number of layers is 2

204 and the dimension of the hidden layer is 256, the model achieves the minimum MSE Loss. Fig.
205 S3 shows the sensitivity test results of model loss varying with different batch size settings,
206 indicating that a batch size of 64 is optimal. Based on the model's MSE loss under different
207 hyperparameter configurations, the best-fitting model can be selected.

208 The Adam optimization algorithm controls the learning rate, which can design
209 independent adaptive learning rates for different parameters. The three initialization parameters
210 ϵ , ρ_1 , and ρ_2 of the Adam algorithm are set to be 0.0001, 0.9, and 0.99, respectively. For the
211 epoch, its size is controlled by the early stop method. The early stop method monitors the
212 change of the model's loss function on the validation set during the training process and stops
213 the model training immediately when the validation loss of the model starts to become larger.
214 Due to the fluctuation of the loss function, a threshold p is set for the early stopping method in
215 practice, and when the validation loss of the model becomes large for p consecutive epochs,
216 the model is rolled back to the lowest validation loss and the training is stopped, and the
217 threshold p is set to 10 in this paper. Fig. S4 shows a typical learning curve of the MSE loss in
218 training and validation data sets for different learning steps in training an optimal model. Such
219 diagnostics can be used to avoid the model overfitting.

220 **2.5 The importance of the model input feature**

221 Permutation feature importance is a technique used to assess the significance of each input
222 feature in a machine-learning model (Altmann et al., 2010). The core idea is to evaluate the
223 impact of each feature on model performance by randomly shuffling its values and observing
224 the resulting change in the model's accuracy. In this study, for each input feature of the GeoNet,
225 we iteratively shuffle its value independently while keeping other features unchanged, and then
226 observe the model prediction on the modified input. The difference in the model prediction
227 performance between using the original and shuffling input quantifies the feature's importance.
228 Here, we measure the relative importance of each input feature using the metric of $1-R^2$, due

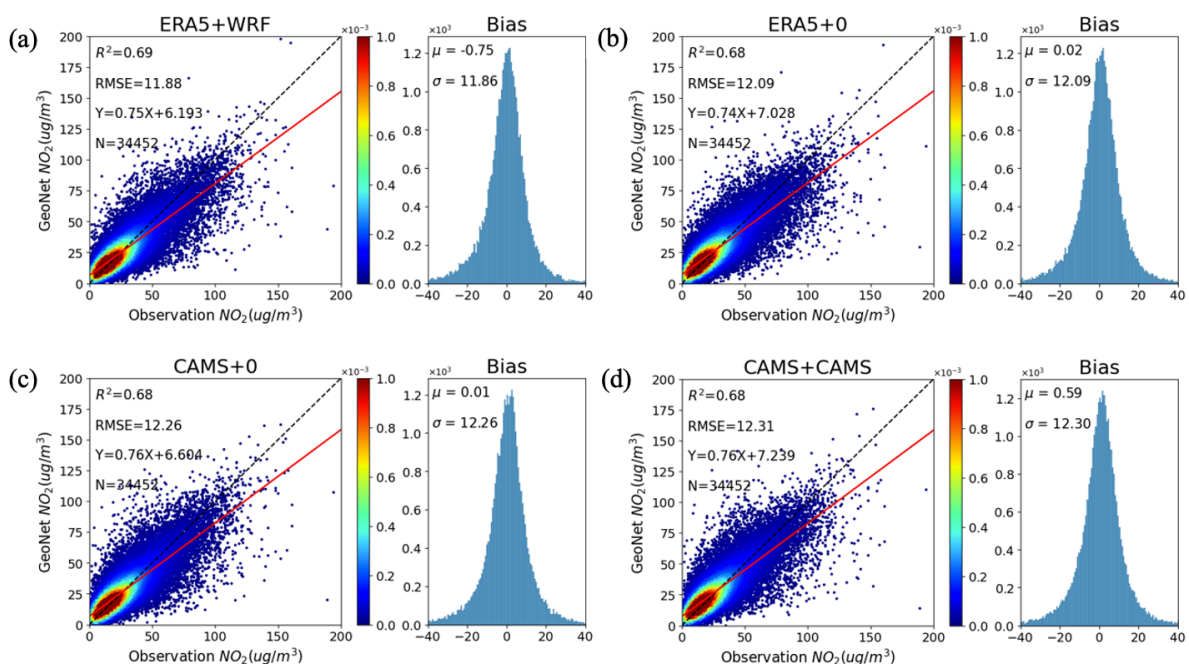
229 to its good standardized and indicative ability (Zhang et al., 2022). Generally, a larger
230 performance drop indicates greater importance, as the model heavily relies on that feature for
231 predictions. Conversely, smaller drops or increases suggest the feature may be less crucial or
232 redundant. By permuting the input feature array based on the different spatial and temporal
233 domains, we can gain a deeper understanding of how feature importance varies spatially and
234 temporally. For example, the relative importance of one meteorology variable may vary with
235 different diurnal, weekly, and monthly cycles, revealing the variability of its impact on the
236 predicted NO₂ levels.

237 **3 Results and Discussion**

238 **3.1 Model performance**

239 Based on the GeoNet model and necessary input data (refer to section 2), we have
240 achieved preliminary predictions of near-surface NO₂ concentration with full spatial coverage
241 and a spatial resolution of 0.1 degrees over eastern China, at four-hour intervals over the next
242 24 hours. In this study, we first tested the impact of using reanalysis and forecast meteorology
243 datasets and filling in missing values in satellite observation data on the model predictions. The
244 reanalysis datasets usually have higher precision than the forecast. Previous studies revealed
245 that the accuracy of the information on meteorology and chemical composition significantly
246 affects the performance of machine learning models in estimating air pollutant concentrations
247 (Zuo et al., 2023; Wang et al., 2024). Due to the shielding effect of clouds, a considerable
248 proportion of missing values may even exist in satellite NO₂ observations. Recent air quality
249 big-data research usually requires the gap-filling of missing satellite data before inputting it
250 into the machine learning model, either by spatial interpolation or regression techniques (Kim
251 et al., 2021). We tested three methods for handling missing data, such as setting them to a fill
252 value of zero, or replacing them by real-time CAMS simulated NO₂, or WRF-Chem simulated
253 NO₂ results (not real-time, but with higher precision).

254 The comparison results to the validation datasets indicate that the scenario using CAMS
 255 meteorology datasets and replacing missing satellite NO₂ data with fill-values (Fig. 2c),
 256 corresponds to a modest NO₂ prediction performance with $R^2=0.68$ and $RMSE=12.26 \mu\text{g}/\text{m}^3$.
 257 In contrast, the configuration scenario using ERA-5 reanalysis meteorology and imputing with
 258 WRF-Chem simulations (Fig. 2a), corresponds to the best prediction performance of $R^2=0.69$
 259 and $RMSE=11.88 \mu\text{g}/\text{m}^3$. This may indicate that the importance of satellite missing data
 260 imputation may be diminished by cloud mask inputs, especially since the model can extract
 261 informative features from spatial and temporal neighboring inputs. To compromise between
 262 the performance of real-time and accuracy, we selected the configuration scenario of using
 263 CAMS meteorology and imputing with CAMS NO₂ (Fig. 2d) for subsequent discussion and
 264 operational forecasting, with an $R^2=0.68$ and $RMSE=12.31 \mu\text{g}/\text{m}^3$. In summary, the use of
 265 higher-precision meteorology and filling missing NO₂ data enhances the model's prediction
 266 accuracy on the validation dataset, but to a rather limited extent. This suggests that, unlike
 267 previous machine learning techniques, GeoNet can effectively adapt to three-dimensional
 268 inputs of varying accuracy and type, fully explore the spatiotemporal correlation of data
 269 features, and demonstrate strong model generalization capabilities.



270

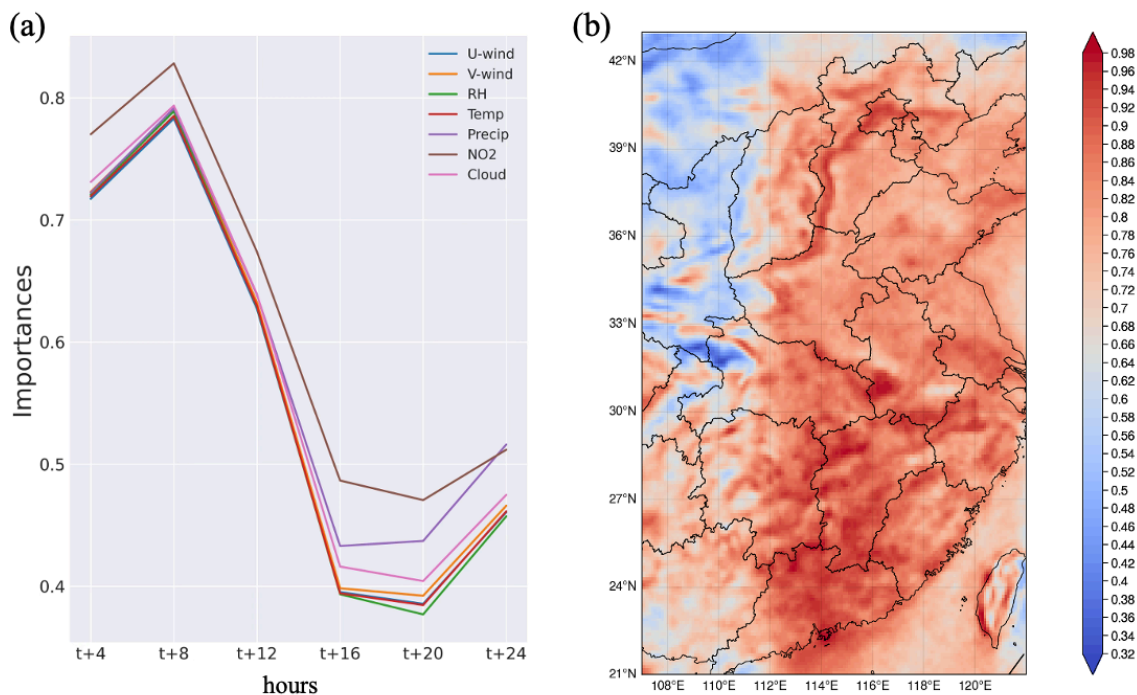
271 **Figure 2.** The GeoNet prediction performance of the surface NO₂ concentration compared to the validation
272 samples, based on different input datasets of meteorology and atmospheric composition: (a) use ERA5
273 meteorology and fill satellite measurement gaps with WRF-Chem simulated NO₂; (b) use ERA5
274 meteorology and NO₂ fill-value of zero for over gaps; (c) use CAMS meteorology and NO₂ fill-value of zero
275 for gaps; (d) use CAMS meteorology and CAMS NO₂. The left plot shows the scatter comparisons between
276 GeoNet predictions and site observations, while the right plot shows the bias distribution between the two.

277 Figs. S5-S8 provide an overview of the major metrics (e.g., R², RMSE, MAE, and MPE)
278 of GeoNet prediction performance varying with prediction hours from t+4h to t+24h in
279 different months. The results indicate that the model exhibits a higher correlation in NO₂
280 forecast during the spring and winter seasons compared to the summer, while the RMSE errors
281 show the opposite trend. This could be attributed to much higher NO₂ pollution levels in winter
282 months. Additionally, GeoNet's NO₂ prediction errors gradually increase during the next 24
283 hours, particularly after t+20h. This is primarily due to the short lifetime of atmospheric NO₂,
284 leading to a diminishing constraint from historical observational data on future NO₂ predictions.
285 Similar phenomena are also observed in machine learning or model-assisted weather forecasts
286 (Andersson et al., 2021).

287 To assess the GeoNet model's performance for short-term pollution events, we compared
288 it with near-surface NO₂ from CAMS forecasts, and in situ observations from CNEMC ground
289 stations. Fig. S9 illustrates the daily time series of t+4h NO₂ from GeoNet, CAMS, and
290 CNEMC for three typical sites in Beijing, Shanghai, and Guangzhou in 2021. As shown from
291 the plot, NO₂ predictions by both GeoNet and CAMS generally agreed with the variation trends
292 of CNEMC measurement. However, CAMS forecasts systematically overestimate the surface
293 NO₂ concentration by 100%, possibly resulting from the biases in the NO_x emission inventory
294 (Douros et al., 2023). Compared to CAMS, the GeoNet prediction closely aligns with the
295 ground-truth observations at CNEMC sites over eastern China, with an overall R² > 0.5 and
296 mean bias < 5 µg/m³ for polluted regions (see Fig. S10 and S11, respectively).

297 **3.2 Main factors in NO₂ forecast and their implications**

298 Previous physics-based numeric models of air quality prediction, e.g., the CAMS global
 299 forecast model and the regional WRF-CMAQ model (Liu et al., 2023; Kumar et al., 2021;
 300 Kuhn et al., 2024), can simulate the atmospheric physical and chemical processes (such as
 301 advection, diffusion, deposition, and chemical reactions) by solving the atmospheric equations.
 302 Recent data assimilation techniques further take real-time monitoring data from satellite and
 303 ground-based platforms as model constraints to better predict air quality variables (Inness et
 304 al., 2022). Compared with physics-based models, “black-box” models such as the deep learning
 305 technique usually lack interpretability and explainability (Zhang and Zhu, 2018). This hinders
 306 the understanding and implications for predicting air quality variables such as NO₂. Here, we
 307 measure the relative importance of each input feature on the NO₂ forecast accuracy, by
 308 iteratively permuting the input array and observing its influences on the model prediction.

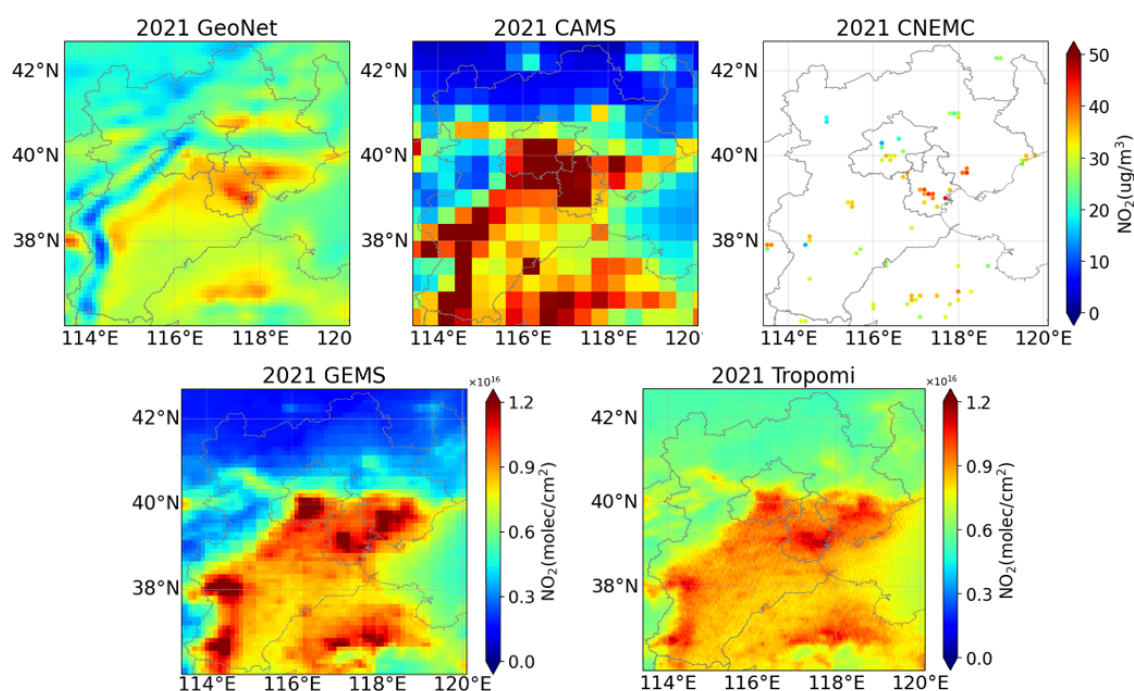


309 **Figure 3.** (a) The overall relative importance of different input features such as wind, surface pressure,
 310 satellite NO₂, and cloud mask, in GeoNet NO₂ forecast, varying with different hour steps from t+4h to t+24h.
 311 (b) The spatial distribution of the relative importance of satellite NO₂ measurements in the GeoNet NO₂
 312 forecast in 2021.
 313

314 Fig. 3a presents the relative importance ($1-R^2$) of different input features varying with
 315 prediction hour steps from t+4h to t+24h. The geostationary satellite NO₂ measurements play

316 the highest role in predicting surface NO₂ levels of the next day, although it degrades after t+8h.
 317 Other meteorological input features also show a major impact on NO₂ prediction performance.
 318 The significance of the different input variables remained generally consistent across seasons,
 319 with minor variations (as shown in Fig. S12). By permutating the input array for each ground
 320 pixel, Fig. 3b derived the spatial distribution of the relative importance of geostationary satellite
 321 NO₂ in the predicting performance. Overall, satellite NO₂ has a higher impact in densely
 322 populated areas experiencing severe air pollution, such as the Pearl River Delta, Yangtze River
 323 Delta, and Jianghuai Plain, than in western China. Such results highlight the underappreciated
 324 role of satellite NO₂ measurements with high spatial and temporal coverage in air pollution
 325 forecasts.

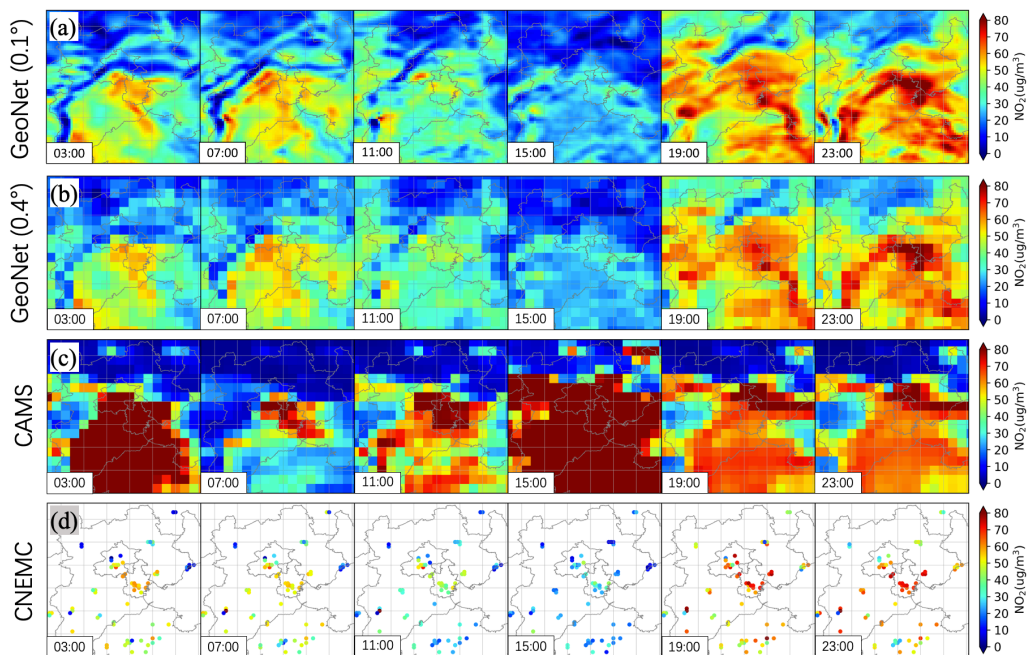
326 3.3 NO₂ pollution episodes and health exposure forecast



327
 328 **Figure 4.** The comparisons of annual surface NO₂ concentrations from GeoNet, CAMS, and CNEMC,
 329 respectively, (in the top panel), as well as the tropospheric NO₂ column observations from GEMS and
 330 TROPOMI over East China in 2021 (in the bottom panel).

331 Beyond its prediction accuracy, GeoNet exhibits a pronounced advantage in spatial
 332 coverage and resolution, allowing for capturing finer-scale details in the pollutant distribution.

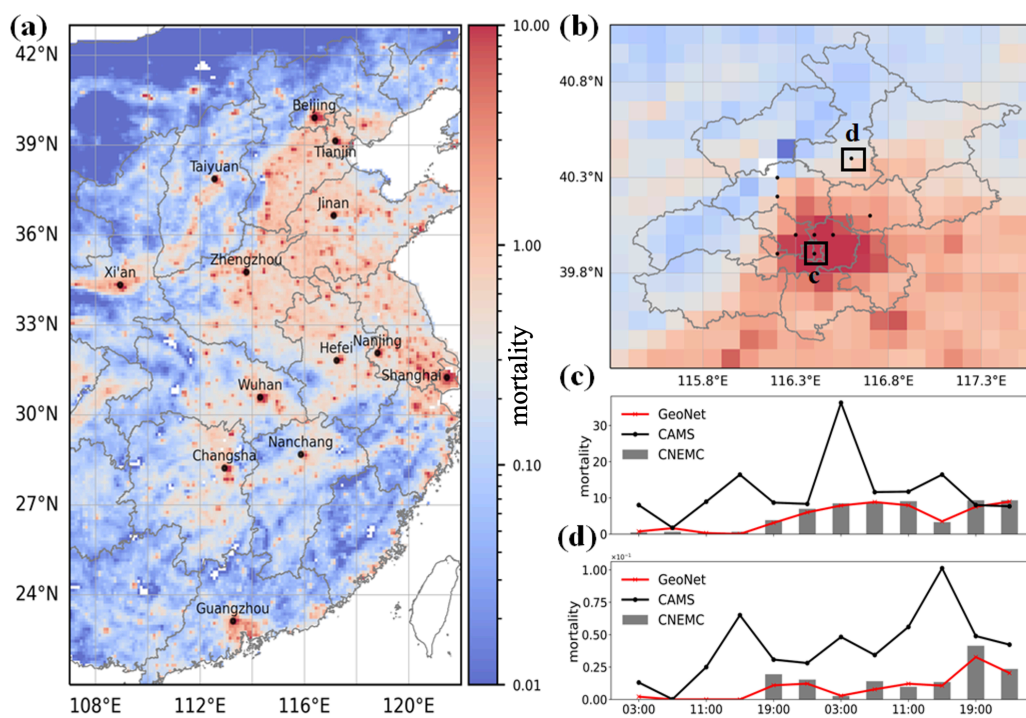
333 Illustrated in Fig. 4, GeoNet demonstrates remarkable performance in predicting spatial
 334 nuances of NO₂ pollution, particularly when contrasted with ground-based and satellite
 335 observations. During a typical winter NO₂ pollution event (as shown in Fig. 5), GeoNet
 336 accurately simulates a significant decrease in concentrations at 11:00 and 15:00, probably led
 337 by intense photochemical activity in the daytime, coincident with ground-based observations.
 338 It also outperforms CAMS in predicting NO₂ variations throughout the day. The GeoNet model
 339 also retains the distributional differences in NO₂ concentrations between urban and rural areas,
 340 consistent with emission source characteristics and satellite observations. The suboptimal
 341 performance of CAMS predictions can be attributed to insufficient observational constraints
 342 and the use of outdated emission inventories (Douros et al., 2023). In the European region, the
 343 assimilation of TROPOMI observations into CAMS forecasts significantly improves the
 344 simulation accuracy of near-surface NO₂ concentrations and tropospheric column densities
 345 (Inness et al., 2019). Neural network methods, similar to GeoNet, could be used to correct and
 346 downscale forecast results by existing models (Baghanam et al., 2024). This approach holds
 347 promise for achieving operational air quality forecasts that balance efficiency and accuracy.



348

349 **Figure 5.** The spatial distribution comparisons of surface NO₂ concentration between (a) GeoNet prediction
 350 at the original resolution of 0.1°, (b) GeoNet prediction resampled to the CAMS resolution of 0.4°, (c) CAMS
 351 prediction, and (d) ground-based CNEMC site measurements. Note that the results are presented for different
 352 continuing local hours (labeled text in the subplot) on 23 November 2021.

353 In this study, we used a simplified linearized risk model for the short-term NO₂ exposure
 354 (Meng et al., 2021; Zhang et al., 2022) to calculate the distribution of all-cause mortality risks
 355 based on GeoNet NO₂ predictions (see Fig. 6). Short-term NO₂ exposure leads to remarkable
 356 regional differences in all-cause mortality, which are mainly concentrated in highly polluted
 357 and densely populated urban areas. For both urban and suburban locations in Beijing (see Fig.
 358 6c-d), GeoNet-based NO₂ pollution exposure predictions are more consistent with actual in situ
 359 observations than the CAMS forecasts. Current air quality health indices forecasting based on
 360 limited station data has significant gaps, making it difficult to meet the refined needs for
 361 different populations in urban, suburban, and rural areas. Integrating GeoNet forecasts based
 362 on hourly geostationary satellite observations can support spatially comprehensive and fine-
 363 scale air quality health risk prediction. This, in turn, guides managing the risks of air pollution
 364 exposure-related diseases in sensitive populations and communities.



365

366 **Figure 6.** Mortality risk of short-term NO₂ exposure based on the GeoNet prediction on November 23, 2021.
367 (a) mean mortality due to the predicted NO₂ exposure in East China; (b) a zoom-in map over Beijing and its
368 neighboring area; (c) and (d) are comparisons of mortality estimation over the Beijing urban and rural
369 regions (the rectangle areas presented in b), respectively, based on different NO₂ exposure prediction among
370 GeoNet, CAMS, and CNEMC.

371 **4 Conclusion**

372 The GeoNet model utilizes the unprecedented hourly air quality observations from
373 geostationary satellites and resolves nonlinear associations in spatiotemporal proximity across
374 multiple data sources. It achieves seamless short-term regional air quality predictions,
375 exhibiting significant performance advantages over existing machine-learning air quality
376 prediction models. To strike a balance between real-time and accuracy requirements, we
377 evaluated the impact of using reanalysis- and forecast-based meteorology datasets, as well as
378 imputing the missing values of satellite NO₂. The findings reveal that the GeoNet model
379 demonstrates robust generalization across diverse datasets, with minimal fluctuations in
380 prediction performance. Overall, the model achieves an RMSE of 12.31 µg/m³ and an R² of
381 0.68 in predicting NO₂ concentrations every 4 hours for the next 24 hours. However, validation
382 accuracy notably diminishes after t+16h within the next 24 hours, with stronger predictive
383 correlations observed in seasons characterized by severe pollution, such as spring and winter,
384 compared to summer. The variation of the model forecasting performance also shows that
385 accurate prediction for longer time windows and heavy pollution events is still a major
386 difficulty. This may be due to the high level of uncertainty in emissions and meteorology. In
387 the future, a combination of higher resolution and more accurate multi-source data constraints,
388 as well as machine learning models coupled with atmospheric physical mechanisms, may be
389 needed to improve the existing forecasts.

390 Compared to traditional chemical model forecasts and data assimilation predictions, the
391 GeoNet model handles various data sources, including meteorological simulations and air
392 quality observations, and more accurately captures spatial intricacies of air pollution evolution.

393 The GeoNet framework elucidated in this study forecasts short-term near-surface NO₂
394 concentrations and demonstrates transferable learning potentials for predicting other pollutants.
395 This work also has important implications for the prediction of near-surface O₃ and particulate
396 matter. For example, the integration of using vertical O₃ profiles from the GEMS satellite, in
397 particular near-surface layer concentrations, and their joint observations of important O₃
398 precursors including NO₂ and HCHO, is expected to significantly improve the uncertainty of
399 existing estimates of near-surface air pollution. This study underscores the pivotal role of next-
400 generation stationary satellite observations of air pollution constituents in air quality
401 forecasting, with the potential to advance operational air quality forecasting and mitigate
402 associated health risks by integrating machine learning technologies.
403

404 **Data and code availability.** The GEMS NO₂ v2.0 data is available from the National Institute
405 of Environmental Research (NIER) of South Korea (<https://nesc.nier.go.kr/en/html/index.do>,
406 last access: December 10, 2023). We downloaded the NO₂ measurements from the CNEMC
407 real-time air quality platform (<https://air.cnemc.cn:18007/>, last access: Jun 8, 2023). ERA-5
408 reanalysis meteorological data is obtained from the European Center for Medium-Range
409 Weather Forecasts (<https://climate.copernicus.eu/climate-reanalysis>, last access: December 8,
410 2023). CAMS forecast of meteorological and atmospheric NO₂ datasets are retrieved from the
411 CAMS Atmosphere Data Store (<https://ads.atmosphere.copernicus.eu/>, last access: December
412 8, 2023). The source codes of the GeoNet model, surface NO₂ prediction, and necessary input
413 data can be obtained from Chengxin Zhang (zcx2011@ustc.edu.cn) upon reasonable request.
414

415 **Contributions:** C.Z. implemented the GeoNet model and analyzed the data. C.L. supervised
416 the study. C.Z. wrote the manuscript with input from all co-authors.
417

418 **Competing interests:** The contact author has declared that none of the authors has any
419 competing interests.
420

421 **Acknowledgments.** This study was supported by the National Natural Science Foundation of
422 China (Nos. 42225504, 62305322, and 42375120), the National Key Research and
423 Development Program of China (Nos. 2022YFC3700100 and 2023YFC3706104), the
424 Fundamental Research Funds for the Central Universities (Nos. YD2090002021 and
425 WK2090000038) and the New Cornerstone Science Foundation through the XPLOER
426 PRIZE (2023-1033).
427

428 **References**

- 429 Altmann, A., Tolosi, L., Sander, O., and Lengauer, T.: Permutation importance: a corrected
430 feature importance measure, *Bioinformatics*, 26, 1340-1347, 10.1093/bioinformatics/btq134,
431 2010.
- 432 Andersson, T. R., Hosking, J. S., Pérez-Ortiz, M., Paige, B., Elliott, A., Russell, C., Law, S.,
433 Jones, D. C., Wilkinson, J., and Phillips, T.: Seasonal Arctic sea ice forecasting with
434 probabilistic deep learning, *Nat Commun*, 12, 5124, 2021.
- 435 Baghanam, A. H., Nourani, V., Bejani, M., Pourali, H., Kantoush, S. A., and Zhang, Y.: A
436 systematic review of predictor screening methods for downscaling of numerical climate
437 models, *Earth-Science Reviews*, 104773, 2024.
- 438 Bi, K., Xie, L., Zhang, H., Chen, X., Gu, X., and Tian, Q.: Accurate medium-range global
439 weather forecasting with 3D neural networks, *Nature*, 1-6, 2023.
- 440 Boukabara, S.-A., Krasnopolsky, V., Penny, S. G., Stewart, J. Q., McGovern, A., Hall, D.,
441 Ten Hoeve, J. E., Hickey, J., Allen Huang, H.-L., and Williams, J. K.: Outlook for exploiting
442 artificial intelligence in the earth and environmental sciences, *B Am Meteorol Soc*, 1-53,
443 2020.
- 444 Campbell, P. C., Tang, Y., Lee, P., Baker, B., Tong, D., Saylor, R., Stein, A., Huang, J.,
445 Huang, H.-C., and Strobach, E.: Development and evaluation of an advanced National Air
446 Quality Forecasting Capability using the NOAA Global Forecast System version 16, *Geosci
447 Model Dev*, 15, 3281-3313, 2022.
- 448 Chan, K. L., Valks, P., Heue, K.-P., Lutz, R., Hedelt, P., Loyola, D., Pinardi, G., Van
449 Roozendael, M., Hendrick, F., and Wagner, T.: Global Ozone Monitoring Experiment-2
450 (GOME-2) daily and monthly level-3 products of atmospheric trace gas columns, *Earth Syst
451 Sci Data*, 15, 1831-1870, 2023.

452 Douros, J., Eskes, H., van Geffen, J., Boersma, K. F., Compernelle, S., Pinardi, G.,
453 Blechschmidt, A.-M., Peuch, V.-H., Colette, A., and Veefkind, P.: Comparing Sentinel-5P
454 TROPOMI NO₂ column observations with the CAMS regional air quality ensemble, *Geosci*
455 *Model Dev*, 16, 509-534, 2023.

456 Du, S., Li, T., Yang, Y., and Horng, S. J.: Deep Air Quality Forecasting Using Hybrid Deep
457 Learning Framework, *IEEE Transactions on Knowledge and Data Engineering*, 33, 2412-
458 2424, 10.1109/TKDE.2019.2954510, 2021.

459 Fino, A., Vichi, F., Leonardi, C., and Mukhopadhyay, K.: An overview of experiences made
460 and tools used to inform the public on ambient air quality, *Atmosphere-Basel*, 12, 1524,
461 2021.

462 Guarin, J. R., Jägermeyr, J., Ainsworth, E. A., Oliveira, F. A., Asseng, S., Boote, K., Elliott,
463 J., Emberson, L., Foster, I., and Hoogenboom, G.: Modeling the effects of tropospheric ozone
464 on the growth and yield of global staple crops with DSSAT v4. 8.0, *Geosci Model Dev*, 17,
465 2547-2567, 2024.

466 Hersbach, H., Bell, B., Berrisford, P., Hirahara, S., Horányi, A., Muñoz-Sabater, J., Nicolas,
467 J., Peubey, C., Radu, R., Schepers, D., Simmons, A., Soci, C., Abdalla, S., Abellan, X.,
468 Balsamo, G., Bechtold, P., Biavati, G., Bidlot, J., Bonavita, M., De Chiara, G., Dahlgren, P.,
469 Dee, D., Diamantakis, M., Dragani, R., Flemming, J., Forbes, R., Fuentes, M., Geer, A.,
470 Haimberger, L., Healy, S., Hogan, R. J., Hólm, E., Janisková, M., Keeley, S., Laloyaux, P.,
471 Lopez, P., Lupu, C., Radnoti, G., de Rosnay, P., Rozum, I., Vamborg, F., Villaume, S., and
472 Thépaut, J.-N.: The ERA5 global reanalysis, *Q J Roy Meteor Soc*, 146, 1999-2049,
473 <https://doi.org/10.1002/qj.3803>, 2020.

474 Hong, C., Zhang, Q., Zhang, Y., Davis, S. J., Tong, D., Zheng, Y., Liu, Z., Guan, D., He, K.,
475 and Schellnhuber, H. J.: Impacts of climate change on future air quality and human health in
476 China, *Proceedings of the national academy of sciences*, 116, 17193-17200, 2019.

477 Hsu, C. H., Henze, D. K., Mizzi, A. P., González Abad, G., He, J., Harkins, C., Naeger, A.
478 R., Lyu, C., Liu, X., and Chan Miller, C.: An Observing System Simulation Experiment
479 Analysis of How Well Geostationary Satellite Trace-Gas Observations Constrain NO_x
480 Emissions in the US, *Journal of Geophysical Research: Atmospheres*, 129, e2023JD039323,
481 2024.

482 Inness, A., Aben, I., Ades, M., Borsdorff, T., Flemming, J., Jones, L., Landgraf, J.,
483 Langerock, B., Nedelec, P., and Parrington, M.: Assimilation of S5P/TROPOMI carbon
484 monoxide data with the global CAMS near-real-time system, *Atmos Chem Phys*, 22, 14355-
485 14376, 2022.

486 Inness, A., Flemming, J., Heue, K. P., Lerot, C., Loyola, D., Ribas, R., Valks, P., van
487 Roozendaal, M., Xu, J., and Zimmer, W.: Monitoring and assimilation tests with TROPOMI
488 data in the CAMS system: near-real-time total column ozone, *Atmos Chem Phys*, 19, 3939-
489 3962, 10.5194/acp-19-3939-2019, 2019.

490 Irrgang, C., Boers, N., Sonnewald, M., Barnes, E. A., Kadow, C., Staneva, J., and Saynisch-
491 Wagner, J.: Towards neural Earth system modelling by integrating artificial intelligence in
492 Earth system science, *Nature Machine Intelligence*, 3, 667-674, 2021.

493 Kim, J., Jeong, U., Ahn, M.-H., Kim, J. H., Park, R. J., Lee, H., Song, C. H., Choi, Y.-S.,
494 Lee, K.-H., and Yoo, J.-M.: New era of air quality monitoring from space: Geostationary
495 Environment Monitoring Spectrometer (GEMS), *B Am Meteorol Soc*, 101, E1-E22, 2020.

496 Kim, M., Brunner, D., and Kuhlmann, G.: Importance of satellite observations for high-
497 resolution mapping of near-surface NO₂ by machine learning, *Remote Sens Environ*, 264,
498 112573, ARTN 112573
499 10.1016/j.rse.2021.112573, 2021.

500 Kim, S., Kim, D., Hong, H., Chang, L.-S., Lee, H., Kim, D.-R., Kim, D., Yu, J.-A., Lee, D.,
501 and Jeong, U.: First-time comparison between NO₂ vertical columns from Geostationary

502 Environmental Monitoring Spectrometer (GEMS) and Pandora measurements, *Atmos Meas*
503 *Tech*, 16, 3959-3972, 2023.

504 Kong, L., Tang, X., Zhu, J., Wang, Z. F., Li, J. J., Wu, H. J., Wu, Q. Z., Chen, H. S., Zhu, L.
505 L., Wang, W., Liu, B., Wang, Q., Chen, D. H., Pan, Y. P., Song, T., Li, F., Zheng, H. T., Jia,
506 G. L., Lu, M. M., Wu, L., and Carmichael, G. R.: A 6-year-long (2013-2018) high-resolution
507 air quality reanalysis dataset in China based on the assimilation of surface observations from
508 CNEMC, *Earth Syst Sci Data*, 13, 529-570, 10.5194/essd-13-529-2021, 2021.

509 Kuhn, L., Beirle, S., Kumar, V., Osipov, S., Pozzer, A., Bösch, T., Kumar, R., and Wagner,
510 T.: On the influence of vertical mixing, boundary layer schemes, and temporal emission
511 profiles on tropospheric NO₂ in WRF-Chem—comparisons to in situ, satellite, and MAX-
512 DOAS observations, *Atmos Chem Phys*, 24, 185-217, 2024.

513 Kumar, V., Remmers, J., Beirle, S., Fallmann, J., Kerkweg, A., Lelieveld, J., Mertens, M.,
514 Pozzer, A., Steil, B., and Barra, M.: Evaluation of the coupled high-resolution atmospheric
515 chemistry model system MECO (n) using in situ and MAX-DOAS NO₂ measurements,
516 *Atmos Meas Tech*, 14, 5241-5269, 2021.

517 Lam, R., Sanchez-Gonzalez, A., Willson, M., Wirnsberger, P., Fortunato, M., Alet, F.,
518 Ravuri, S., Ewalds, T., Eaton-Rosen, Z., and Hu, W.: Learning skillful medium-range global
519 weather forecasting, *Science*, 382, 1416-1421, 2023.

520 Li, Y., Xing, C., Peng, H., Song, Y., Zhang, C., Xue, J., Niu, X., and Liu, C.: Long-term
521 observations of NO₂ using GEMS in China: Validations and regional transport, *Science of*
522 *The Total Environment*, 904, 166762, 2023.

523 Lin, Z., Li, M., Zheng, Z., Cheng, Y., and Yuan, C.: Self-attention convlstm for
524 spatiotemporal prediction, *Proceedings of the AAAI conference on artificial intelligence*,
525 11531-11538,

526 Liu, C., Wu, C., Kang, X., Zhang, H., Fang, Q., Su, Y., Li, Z., Ye, Y., Chang, M., and Guo,
527 J.: Evaluation of the prediction performance of air quality numerical forecast models in
528 Shenzhen, *Atmos Environ*, 314, 120058, <https://doi.org/10.1016/j.atmosenv.2023.120058>,
529 2023.

530 Makar, P., Gong, W., Milbrandt, J., Hogrefe, C., Zhang, Y., Curci, G., Žabkar, R., Im, U.,
531 Balzarini, A., and Baró, R.: Feedbacks between air pollution and weather, Part 1: Effects on
532 weather, *Atmos Environ*, 115, 442-469, 2015.

533 Manisalidis, I., Stavropoulou, E., Stavropoulos, A., and Bezirtzoglou, E.: Environmental and
534 health impacts of air pollution: a review, *Frontiers in public health*, 14, 2020.

535 Meng, X., Liu, C., Chen, R., Sera, F., Vicedo-Cabrera, A. M., Milojevic, A., Guo, Y., Tong,
536 S., Coelho, M. d. S. Z. S., and Saldiva, P. H. N.: Short term associations of ambient nitrogen
537 dioxide with daily total, cardiovascular, and respiratory mortality: multilocation analysis in
538 398 cities, *bmj*, 372, 2021.

539 Nguyen, T., Brandstetter, J., Kapoor, A., Gupta, J. K., and Grover, A.: ClimaX: A foundation
540 model for weather and climate, *arXiv preprint arXiv:2301.10343*, 2023.

541 Peuch, V.-H., Engelen, R., Rixen, M., Dee, D., Flemming, J., Suttie, M., Ades, M., Agustí-
542 Panareda, A., Ananasso, C., and Andersson, E.: The Copernicus Atmosphere Monitoring
543 Service: From Research to Operations, *B Am Meteorol Soc*, 103, E2650-E2668, 2022.

544 Sathe, Y., Gupta, P., Bawase, M., Lamsal, L., Patadia, F., and Thipse, S.: Surface and satellite
545 observations of air pollution in India during COVID-19 lockdown: Implication to air quality,
546 *Sustainable cities and society*, 66, 102688, 2021.

547 Shah, V., Jacob, D. J., Li, K., Silvern, R. F., Zhai, S., Liu, M., Lin, J., and Zhang, Q.: Effect
548 of changing NO_x lifetime on the seasonality and long-term trends of satellite-observed
549 tropospheric NO₂ columns over China, *Atmos Chem Phys*, 20, 1483-1495, 2020.

550 Shu, L., Zhu, L., Bak, J., Zoogman, P., Han, H., Liu, S., Li, X., Sun, S., Li, J., and Chen, Y.:
551 Improving ozone simulations in Asia via multisource data assimilation: results from an

552 observing system simulation experiment with GEMS geostationary satellite observations,
553 Atmos Chem Phys, 23, 3731-3748, 2023.

554 Tang, K. T. J., Lin, C., Wang, Z., Pang, S. W., Wong, T.-W., Yu, I. T. S., Fung, W. W. Y.,
555 Hossain, M. S., and Lau, A. K.: Update of Air Quality Health Index (AQHI) and
556 harmonization of health protection and climate mitigation, Atmos Environ, 326, 120473,
557 2024.

558 Van Geffen, J., Eskes, H., Compernelle, S., Pinardi, G., Verhoelst, T., Lambert, J.-C., Sneep,
559 M., Ter Linden, M., Ludewig, A., and Boersma, K. F.: Sentinel-5P TROPOMI NO₂
560 retrieval: impact of version v2. 2 improvements and comparisons with OMI and ground-
561 based data, Atmos Meas Tech, 15, 2037-2060, 2022.

562 Wang, S., Zhang, M., Gao, Y., Wang, P., Fu, Q., and Zhang, H.: Diagnosing drivers of PM
563 2.5 simulation biases in China from meteorology, chemical composition, and emission
564 sources using an efficient machine learning method, Geosci Model Dev, 17, 3617-3629,
565 2024.

566 Zhang, C., Liu, C., Li, B., Zhao, F., and Zhao, C.: Spatiotemporal neural network for
567 estimating surface NO₂ concentrations over north China and their human health impact,
568 Environ Pollut, 119510, 2022.

569 Zhang, Q.-s. and Zhu, S.-C.: Visual interpretability for deep learning: a survey, Frontiers of
570 Information Technology & Electronic Engineering, 19, 27-39, 2018.

571 Zhong, S., Zhang, K., Bagheri, M., Burken, J. G., Gu, A., Li, B., Ma, X., Marrone, B. L.,
572 Ren, Z. J., and Schrier, J.: Machine learning: new ideas and tools in environmental science
573 and engineering, Environ Sci Technol, 55, 12741-12754, 2021.

574 Zuo, C., Chen, J., Zhang, Y., Jiang, Y., Liu, M., Liu, H., Zhao, W., and Yan, X.: Evaluation
575 of four meteorological reanalysis datasets for satellite-based PM_{2.5} retrieval over China,
576 Atmos Environ, 305, 119795, 2023.

577
578